Investigation and Design of a High-Power Flux-Switching Permanent Magnet Machine for Hybrid Electric Vehicles

Wei Hua, Gan Zhang, and Ming Cheng

School of Electrical Engineering, Southeast University, Nanjing 210096, China

Flux-switching permanent magnet (FSPM) machines exhibit high torque density, high efficiency, and robust rotor structure. In this paper, a prototype of a high-power three-phase 12-stator-slot/10-rotor-pole FSPM motor used for hybrid electric vehicles (HEVs) is designed by finite-element analysis (FEA). First, the initial FEA model is improved by gradually taking into account lamination *B–H* curves due to different electrical frequencies, operation temperatures, 3-D end effect, and rotor eccentric. Thereafter, a modular manufacture method of the FSPM motor is discussed with the improved FEA model and validated by experimental measurements. Then, the measured overload capability of the FSPM motor is compared with that of an interior permanent magnet (IPM) motor used in Honda Civic, and the results indicate that the IPM motor exhibits significantly stronger overload capability, which is analyzed in depth from soft-iron materials, cooling conditions, and and so on. Finally, both the merits and demerits of FSPM motor employed for low-voltage and high-current HEV applications are highlighted.

Index Terms—**Finite-element analysis (FEA), flux switching, high power, hybrid electric vehicle (HEV), permanent magnet (PM).**

I. INTRODUCTION

WITH the requirements of reducing emissions and improving fuel economy, electric vehicles and hybrid electric vehicles (HEVs) have attracted increasing attentions [1], where high reliability, large power density, and enough overload capabilities are expected. Meantime, the flux-switching permanent magnet (FSPM) motors have attracted considerable interests for high performance drive applications due to the high torque and power densities [2]–[9]. In addition, since the magnets and armature windings are both located on the stator, a simple and robust rotor structure makes FSPM machines well suited for high-speed applications [10].

In this paper, a modular manufactured low-voltage high-current three-phase FSPM motor used for HEVs is designed by finite-element analysis (FEA). The initial FEA model is improved gradually by taking the lamination *B–H* curves under different electrical frequencies, operation temperature, 3-D end effect, and rotor eccentric into account, respectively. The corresponding influences on electromagnetic performances are investigated in depth, especially for the phase back-electromotive force and electromagnetic torques under rated operations. Compared to the initial FEA model, an overall 40% drop of electromagnetic torque can be found in the improved FEA model that considers the mentioned design factors simultaneously.

Furthermore, the FEA predicted overload capability of the FSPM motor obtained by the improved model is validated by experimental measurements, which are further compared with that of an interior permanent magnet (IPM) motor used as an integrated starter generator (ISG) in Honda Civic. For a fair comparison, the two motors are designed to have the same overall dimensions and operation conditions. Comparison
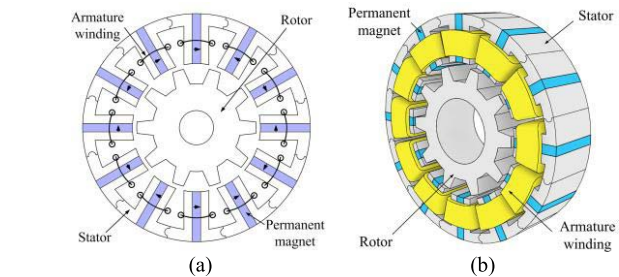
Fig. 1. Topology of the 12-stator-slot/10-rotor-pole FSPM motor. (a) Cross section. (b) 3-D configuration.
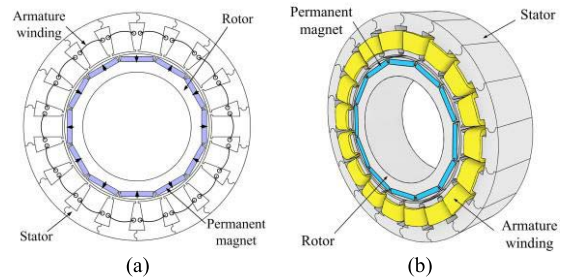

Fig. 2. Topology of the 18-stator-slot/12-rotor-pole IPM motor. (a) Cross section. (b) 3-D configuration.

shows that IPM motor exhibits significantly stronger overload capability, which indicates that in the stator-PM motor, accommodating both PMs and armature windings in the stator may contribute to the unbalanced saturation distributions between stator and rotor, consequently resulting in weak overload capability and lower magnet utilization.

II. MOTOR TOPOLOGIES

Fig. 1 shows the structure of the three-phase 12/10-pole FSPM motor, and Fig. 2 shows the 18/12-pole IPM motor. Both stators are modular manufactured with concentrate armature winding coils adopted. Meanwhile, the magnet volumes in the FSPM motor is obviously larger than that in the IPM motor (with identical stator outer radius and stack length). The detailed design dimensions of the FSPM motor is illustrated in Fig. 3 and listed in Table I.
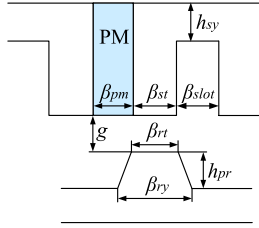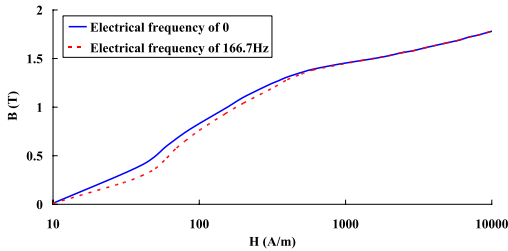
Fig. 3.   Design dimensions of the FSPM motor.

TABLE I
DESIGN SPECIFICATIONS OF THE FSPM MOTOR

| Items	FSPM motor
Base Speed, N_n	1000 rpm
Rated power, P_n	4.8 kW
Magnet remanence, B_r	1.2 T
Turns per coil, n	18
Air-gap length, g	0.9 mm
Stack length, l_a	40 mm
Stator outer diameter, D_{so}	240 mm
Stator split ratio, k_{sio}	0.60
Stator yoke height, h_{sy}	9.4 mm
Stator tooth arc, β_{st}	8.0º
Stator slot arc, β_{slot}	8.0º
Magnet width arc, β_{pm}	6.0º
Rotor tooth arc, β_{rt}	10.5º
Rotor yoke arc, β_{ry}	21º
Rotor yoke tooth height, h_{pr}	17.8 mm

Fig. 4. B–H curves due to different electrical frequencies.

III. DESIGN CONSIDERATIONS OF THE FSPM MOTOR

In this section, the original electromagnetic performance of the FSPM motor is obtained by an initial FEA model (namely Initial). Then, the FEA model is improved by gradually taking into account the B–H curves of iron laminations due to different electrical frequencies, steady-state temperature at rated operation, 3-D end effect, and rotor eccentrics.

A. Lamination B–H Curves

The material of the iron laminations for the FSPM prototype is 50WW600, which is a common material used in normal induction motors in China. Fig. 4 shows the B–H curves under electrical frequency $f_e = 0$ Hz and $f_e = 166.7$ Hz (responding to the rated speed of 1000 r/min). The relative permeability distributions obtained by the initial model ($f_e = 0$ Hz) and improved model ($f_e = 166.7$ Hz) are compared in Figs. 5 and 6. As can be seen, the higher electrical frequency causes lower permeability and deeper saturations, especially for the domains where stator tooth is
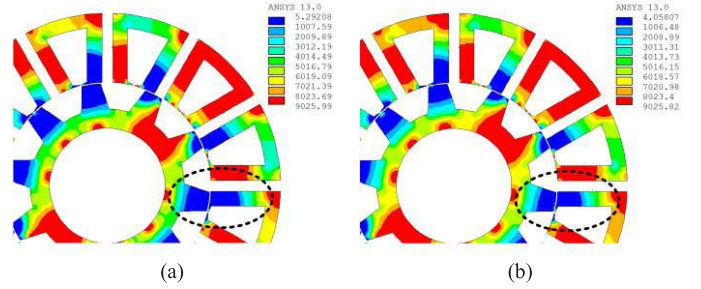
Fig. 5.   Partial open-circuit relative permeability distributions at d-axis. (a) Employing B–H curve of $f_e = 0$ Hz. (b) Employing B–H curve of $f_e = 166.7$ Hz.
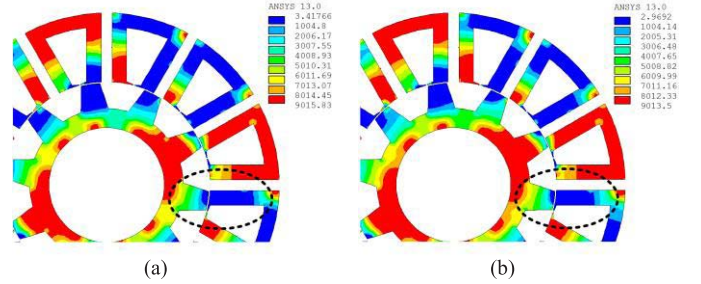
Fig. 6.   Partial rated relative permeability distributions at d-axis. (a) Employing B–H curve of $f_e = 0$ Hz. (b) Employing B–H curve of $f_e = 166.7$ Hz.
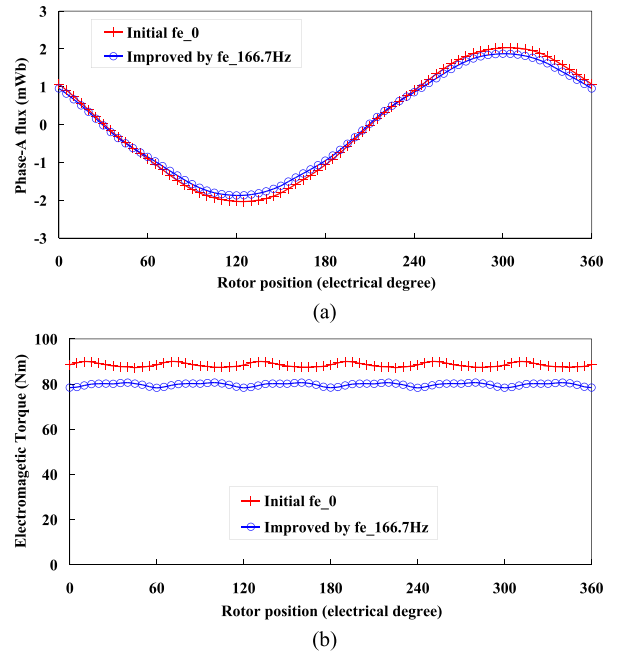
Fig. 7.   Rated electromagnetic performances under $f_e = 0$ Hz and $f_e = 166.7$ Hz. (a) Phase-A fluxes. (b) Electromagnetic torques.

fully overlapped with rotor tooth as marked by dotted circles. In addition, a reduction of 11% can be predicted in both phase PM flux and electromagnetic torques, as shown in Fig. 7.

B. Operation Temperature

In HEV applications with large currents and lower voltage, rated operation temperature is directly related to PM demagnetization, especially in FSPM motors, where the magnets
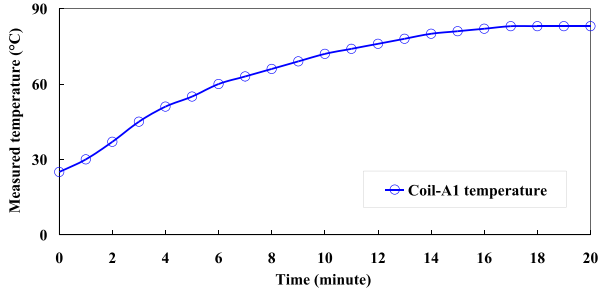
Fig. 8. Measured coil-A1 temperature on the FSPM motor prototype under rated operation condition.
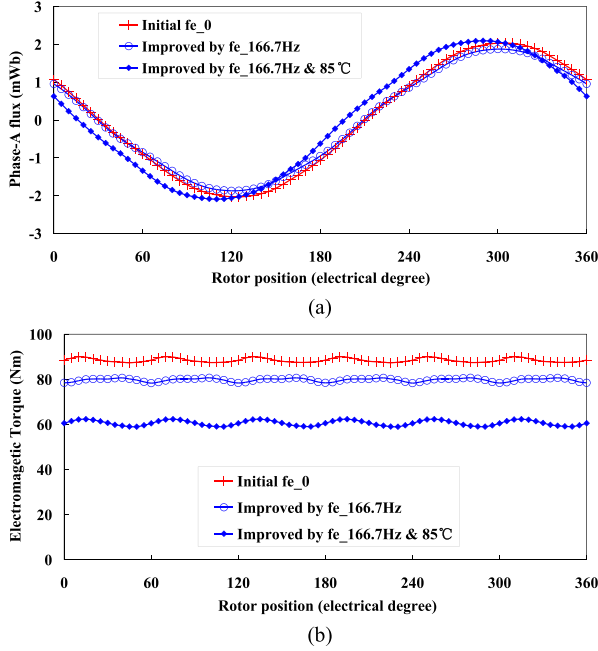

Fig. 10. Rated flux density distributions by FEA method at *d*-axis. (a) 2-D model. (b) 3-D model (half motor).

Fig. 9. Comparisons of FEA predicted rated electromagnetic performances. (a) Phase-A fluxes. (b) Electromagnetic torques.

Fig. 11. 3-D FEA predicted air-gap flux density distributions at *d*-axis.
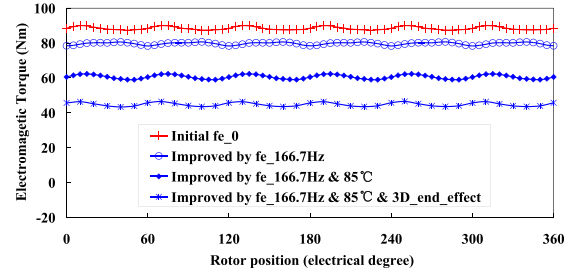
Fig. 12. Comparison of FEA predicted electromagnetic torques.

are surrounded by armature windings. In the linear part of the B–H curve, for temperature below $\sim$100 °C, the PM remanence B_r and coercive force H_c vary linearly with temperature, which can be expressed as [11], [12]

$$B_r = B_{rA} + s_b (T - T_A) \qquad (1)$$

$$H_c = H_{cA} + s_c (T - T_A) \qquad (2)$$

where B_{rA} and H_{cA} are the remanence and coercive force at normal ambient temperature T_A, and s_b and s_c are the slope of B_r- and H_c-temperature characteristics. The typical values of s_b and s_c for NdFeB magnets applied in this paper are -0.11%/°C and -0.62%/°C, respectively. Fig. 8 shows the measured temperature of the armature windings in the FSPM motor prototype under rated operation, and the steady temperature adopted in the initial and improved FEA models are 25 °C (assumed with water-cooling) and 85 °C (measured with air-cooling), respectively. Comparisons of phase-A fluxes and torques obtained by different models can be found in Fig. 9, as can be seen, a significant torque drop is caused by higher temperature. In addition, it should be
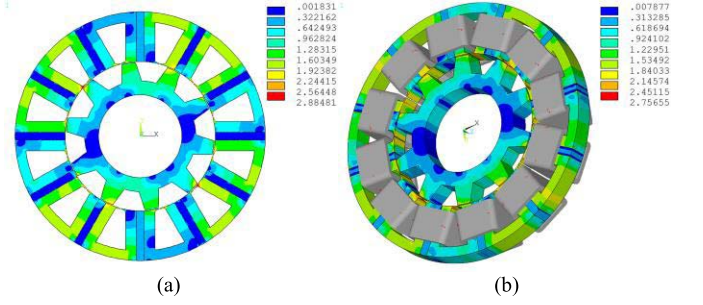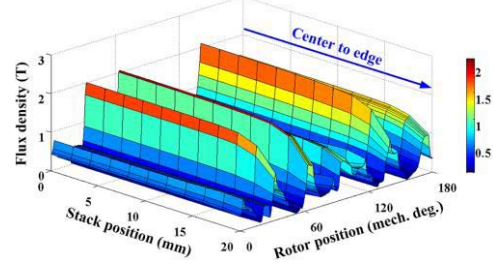
noticed that in Fig. 9(a), both amplitude and phase position of phase-A flux vary with the PM demagnetization, which can be attributed to lower saturation degree and stronger armature reaction. Though the flux amplitude is slightly increased, a reduction of 20 Nm can be found in the electromagnetic torque, since the power factor degrades from 0.61 to 0.46.

C. 3-D End Effect

Since the ratio of stack length to stator outer diameter is only 1/6, the 3-D end effect in the FSPM motor cannot be neglected. Fig. 10 shows the flux density distributions at rated operation obtained by 2-D and 3-D FEA models, respectively. The corresponding 3-D air-gap flux density distributions from axial center to edge is shown in Fig. 11. As can be seen, the air-gap field is evidently weaker near the stack edge, which results in the decreased electromagnetic torques by 22% as shown in Fig. 12, and a lower PM utilization. Additionally, a reduction of 13% is found in open-circuit phase flux when considering 3-D end effect.

D. Rotor Eccentric

A modular manufacturing method could contribute to the rotor eccentric, especially considering the vibrations in
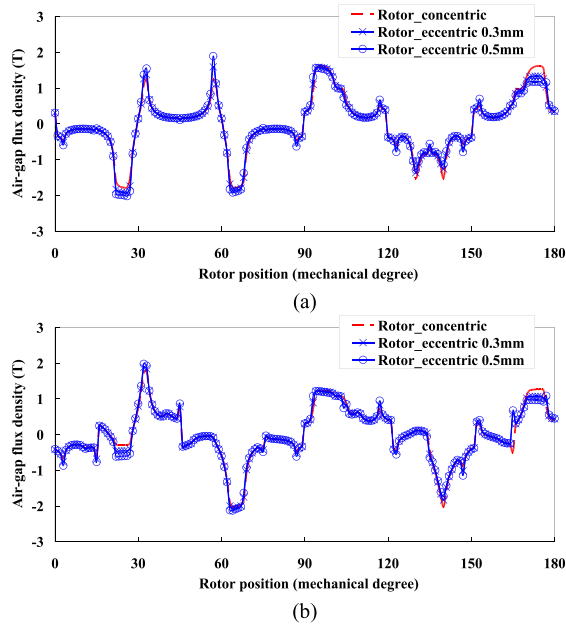
Fig. 13. Comparisons of air-gap flux density distributions at d-axis. (a) Open-circuit operation. (b) Rated operation.
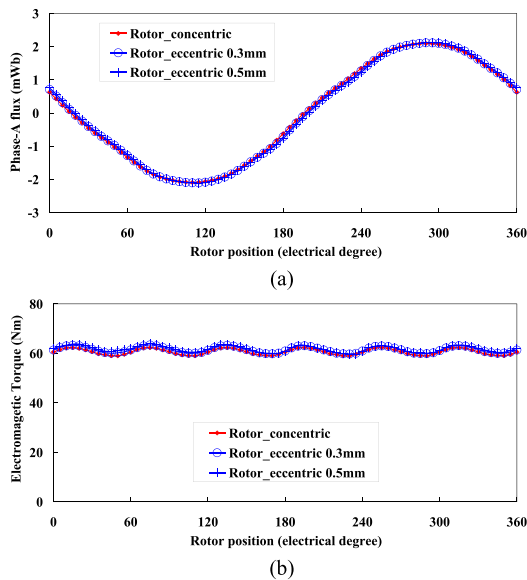

Fig. 14. Comparison of FEA predicted rated electromagnetic performances. (a) Phase-A fluxes. (b) Electromagnetic torques.

Fig. 15. Modular manufactured FSPM motor prototype.

Fig. 16. Comparison of the overload capabilities.

the HEVs. Hence, the performances due to a rotor eccentric of 0.3 and 0.5 mm (distance between rotor axis and stator axis) are compared with that of rotor concentric by neglecting 3-D end effect and unbalanced electromagnetic force. As shown in Figs. 13 and 14, comparisons of both open-circuit and rated operation performances reveal that the influence of rotor eccentric can be neglected (a discrepancy of 1.6%–2% in the phase fluxes and electromagnetic torques).

IV. COMPARISON OF TORQUE CAPABILITIES

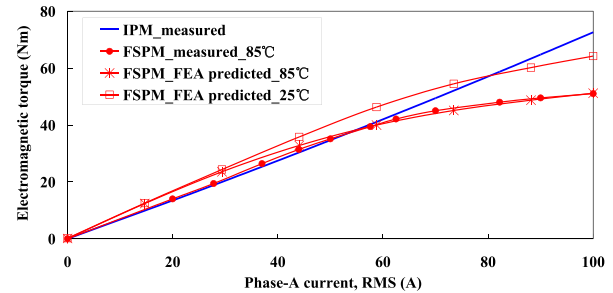A prototype of the FSPM motor is manufactured as shown in Fig. 15. The torque capability of the FSPM motor is compared with the IPM motor in Fig. 16. Cooling conditions

of the FSPM motor under both 25 °C and 85 °C are considered.

First, the experimental measurements of the FSPM motor agree with FEA predictions (considering $B–H$ curves, temperature, and 3-D end effect) with satisfied accuracy. In addition, the discrepancy between measurement and FEA predictions decreases with the increase of armature current, since the consequently enhanced saturations may weaken the influence of manufacturing tolerances such as unsatisfied air gap.

Meanwhile, a higher torque is found in the FSPM motor when phase current is relatively low, but the IPM motor (water cooling) exhibits significantly stronger overload capability. This can be attributed to the balanced saturations distributions between the stator and rotor in the IPM motor, due to specific accommodations of magnet and armature windings that are separated by the air gap. Additionally, the weaker performances of the soft-iron material in the FSPM motor can also contribute to the inferior overload capability.

The comparisons also indicate that a low stack length to diameter ratio may not be employed in the FSPM motor in high-power applications. Since larger diameter requires relatively greater stator split ratio, which could consequently result in lower space-utilization and stronger 3-D end effect.

V. CONCLUSION

A prototype of high-power FSPM motor used for an ISG in the HEVs is designed by FEA. The initial FEA model is improved by gradually taking into account lamination $B–H$ curves due to different electrical frequencies, operation temperatures, 3-D end effect, and rotor eccentric. FEA predicted overload capability of the FSPM motor by the improved model is validated by experimental measurements, which is further compared with that of the IPM motor used in Honda Civic.

It can be summarized as follows.

1) The FSPM motor exhibits a larger torque capability than that of the IPM motor as the armature current is low where the saturation is not severe. However, as the armature current increases, the IPM motor exhibits significantly stronger overload capability due to the fact that the FSPM motor is easier to deep saturation since the complicated stator configurations.

2) The rotor pole number of FSPM motors is a key design parameter since it determines the electrical frequency at rated operation, which has a considerable influence on the iron loss and saturation level.

3) Both the temperature and the ratio of stack length to the stator outer diameter have significant influences on the electromagnetic torque, and hence, the cooling condition should be satisfied for the high current and power applications. Whereas, the influence of a limited rotor eccentric can be neglected.

ACKNOWLEDGMENT

REFERENCES

[1] C. C. Chan, "The state of the art of electric, hybrid, and fuel cell vehicles," *Proc. IEEE*, vol. 95, no. 4, pp. 704–718, Apr. 2007.

[2] E. Hoang, A. H. Ben-Ahmed, and J. Lucidarme, "Switching flux permanent magnet polyphased synchronous machines," in *Proc. 7th Eur. Conf. Power Electron Appl.*, vol. 3. 1997, pp. 903–908.

[3] J. H. Yan, H. Lin, Y. Feng, Z. Q. Zhu, P. Jin, and Y. J. Guo, "Cogging torque optimization of flux-switching transverse flux permanent magnet machine," *IEEE Trans. Magn.*, vol. 49, no. 5, pp. 2169–2172, May 2013.

[4] M. Cheng, W. Hua, J. Zhang, and W. Zhao, "Overview of stator-permanent magnet brushless machines," *IEEE Trans. Ind. Electron.*, vol. 58, no. 11, pp. 5087–5101, Nov. 2011.

[5] Z. Q. Zhu, Y. Pang, D. Howe, S. Iwasaki, R. Deodhar, and A. Pride, "Analysis of electromagnetic performance of flux-switching permanent-magnet machines by nonlinear adaptive lumped parameter magnetic circuit model," *IEEE Trans. Magn.*, vol. 41, no. 11, pp. 4277–4287, Nov. 2005.

[6] W. Hua, M. Cheng, Z. Q. Zhu, and D. Howe, "Analysis and optimization of back emf waveform of a flux-switching permanent magnet motor," *IEEE Trans. Energy Convers.*, vol. 23, no. 3, pp. 727–733, Sep. 2008.

[7] W. Hua and M. Cheng, "Static characteristics of doubly-salient brushless machines having magnets in the stator considering end-effect," *Electr. Power Compon. Syst.*, vol. 36, no. 7, pp. 754–770, Jun. 2008.

[8] W. Hua, M. Cheng, Z. Q. Zhu, W. Zhao, and X. Kong, "Comparison of electromagnetic performance of brushless motors having magnets in stator and rotor," *J. Appl. Phys.*, vol. 103, no. 7, pp. 07F124-1–07F124-3, Apr. 2008.

[9] Z. Q. Zhu and D. Howe, "Electrical machines and drives for electric, hybrid, and fuel cell vehicles," *Proc. IEEE*, vol. 95, no. 4, pp. 746–765, Apr. 2007.

[10] K. T. Chau, C. C. Chan, and C. Liu, "Overview of permanent-magnet brushless drives for electric and hybrid electric vehicles," *IEEE Trans. Ind. Electron.*, vol. 55, no. 6, pp. 2246–2257, Jun. 2008.

[11] T. Sebastian, "Temperature effects on torque production and efficiency of PM motors using NdFeB magnets," *IEEE Trans. Ind. Appl.*, vol. 31, no. 2, pp. 353–357, Mar./Apr. 1995.

[12] P. Zhou, D. Lin, Y. Xiao, N. Lambert, and M. A. Rahman, "Temperature-dependent demagnetization model of permanent magnets for finite element analysis," *IEEE Trans. Magn.*, vol. 48, no. 2, pp. 1031–1034, Feb. 2012.